Photocurable “all-lignocellulose” derived hydrogel nanocomposites for adsorption of cationic contaminants

Sustainable Materials and Technologies 27 (2021) e00243

Contents lists available at ScienceDirect

Sustainable Materials and Technologies

journal homepage: www.elsevier.com/locate/susmat

Photocurable "all-lignocellulose" derived hydrogel nanocomposites for adsorption of cationic contaminants

Giuseppe Melilli [a], Jenevieve Yao [a], Annalisa Chiappone [b,c], Marco Sangermano [b,c], Minna Hakkarainen [a,*]

[a] KTH Royal Institute of Technology, Department of Fibre and Polymer Technology, Teknikringen 56-58, 10044 Stockholm, Sweden
[b] POLITO BIOMedLAB, Politecnico di Torino, Turin, Italy
[c] Department of Applied Science and Technology, Politecnico di Torino, C.so Duca degli Abruzzi 24, 10129 Torino, Italy

ARTICLE INFO

Article history:
Received 18 September 2020
Received in revised form 9 November 2020
Accepted 9 December 2020
Available online xxxx

Keywords:
Carboxymethyl cellulose
Photo-curing
Sodium lignosulfonate
Carbon flakes
Cationic adsorption
Hydrogel

ABSTRACT

Removal of contaminants from wastewater is one key element for the development of sustainable society. Here, innovative "all-lignocellulose" derived photo-curable hydrogel nanocomposites based on methacrylated carboxymethyl cellulose (M-CMC) and lignosulfonate-derived carbonaceous products were successfully designed. The carbon products were synthesized by microwave-assisted hydrothermal carbonization (MAHC), followed by oxidation and methacrylation. This yielded nano-graphene oxide (nGO) and methacrylated nGO (M-nGO). The structure of the carbon products was confirmed by several spectroscopic techniques. The photo-curing process, mechanical properties, swelling degree, adsorption efficiency towards cationic contaminants and recycling efficiency of the produced hydrogel nanocomposites containing different amounts of nGO or M-nGO were evaluated. Rapid photo-curing was demonstrated for all studied compositions. However, the shielding effect caused by the addition of aromatic nGO increased the time required for reaching gel point (8.5–19.5 s, instead of 4.8 s for pure M-CMC). This was partially compensated by the addition of M-nGO, that could participate in the photo-curing process. The photo-cured nanocomposites, M-CMC/nGO and M-CMC/M-nGO, demonstrated good mechanical properties, extremely high swelling degrees, outstanding adsorption capacity (up to 350 and 145 mg/g for MB and Cu(II) adsorption, respectively) and very good recyclability for at least 3 cycles. The designed "all-lignocellulose" derived hydrogel nanocomposites are, thus, promising candidates for wastewater purification to ensure access to clean water.

1. Introduction

Water pollution is a critical environmental issue for modern society. Soluble organic compounds, dyes and heavy metal ions are pollutants produced by cosmetic, petroleum, dyeing, pharmaceutical and textile industries. Although the total amount of global water on Earth does not change with time, the demand is expected to grow significantly over the next two decades for all three sectors – industry, domestic and agriculture [1]. Thus, wastewater recycling and decontamination are the two possible options to meet the global water requirements [2]. Numerous techniques have been employed for wastewater treatment, including membrane filtration [3,4], ion-exchange [5], electrochemical [6], photo-degradation [7], coagulation-flocculation [8], and adsorption [9–14]. Compared with other techniques, adsorption is an efficient process with fast kinetics and appreciable removal capacity [15,16]. Bio-based sorbents are promising candidates for adsorption of dyes and heavy metal ions due to their renewability, abundance, low-cost, non-toxicity, often easy regeneration, and potential biodegradability [17].

Bio-based hydrogels are three-dimensional hydrophilic networks composed of chemically and/or physically crosslinked natural polymers. Hydrogels are characterized by high swelling ability enabling use as superior adsorbents. Polysaccharide-based hydrogels such as cellulose, starch, chitosan and sodium alginate have been widely employed in environmental applications including desalination [18,19] and heavy metal ion and dye removal [20–23]. Carboxymethyl cellulose (CMC) is a biocompatible and biodegradable anionic polysaccharide obtained by partial substitution of cellulose hydroxyl groups with carboxyl groups. Due to the chelating properties of the carboxyl and hydroxyl groups, CMC hydrogels have been widely employed for adsorption of positively charged heavy metal ions, e.g. Cu(II), Pb(II), Cd(II), and cationic methylene blue (MB) dye [24–29]. CMC can also be functionalized with methacrylate groups to design photo-curable bio-based resins for light-assisted 3D printing [30].

Recently, graphene oxide (GO) has attracted a lot of attention as a promising adsorbent. The high potential of GO derives from the ultra-large specific surface area and high concentration of negatively charged groups on the surface, which results in affinity for wide range of

* Corresponding author.
E-mail address: minna@kth.se (M. Hakkarainen).

https://doi.org/10.1016/j.susmat.2020.e00243

pollutants including heavy metal ions, and dyes [12,31–34]. GO has also been extensively used as a component in hydrogels based on carboxymethyl cellulose [24], chitosan [35], konjac glucomannan [36], polyvinyl alcohol [37], and guar gum [38]. Graphite is the primary source of graphene and GO, but the production process is harsh and requires high graphitization temperature and strong chemicals [39]. An alternative and sustainable strategy towards the production of carbonaceous materials involves the exploitation of low-value resources such as biomass. Biochar is a stable aromatic porous carbon-rich material obtained by pyrolysis of biomass. Due to the extraordinary physiochemical properties, biochar and biochar-based materials have been reported as efficient adsorbents for removal of organic and inorganic pollutants [40]. Microwave-assisted hydrothermal carbonization (MAHC), on the other hand, allows the conversion of biomass to high-value carbon materials under aqueous conditions at moderate temperatures [13,41–44]. In our previous communication [44], MAHC of lignosulfonate was investigated. It was shown that the produced elongated carbonaceous structures (denoted as carbon flakes) contained nano-graphitic domains. We also demonstrated the excellent adsorption capacity of lignin-derived porous carbon nanocomposites for heavy metal ions and cationic dyes [13]. Therefore, we anticipated that powerful "all-lignocellulose" derived hydrogel nanocomposite adsorbents could be designed by combining the lignosulfonate derived carbon products with rapidly photo-curable methacrylated carboxymethyl cellulose (M-CMC) superabsorbent [31]. Microwave-assisted hydrothermal carbonization was employed for the conversion of sodium lignosulfonate (SLS) to carbon flakes, which were further oxidized to small nano-graphene oxide (nGO) carbon dots and functionalized with photo-reactive methacrylate groups (M-nGO). Two classes of M-CMC hydrogel nanocomposites were fabricated through modification by nGO or M-nGO and evaluated for the photo-curing process, mechanical properties, swelling degree, adsorption efficiency towards cationic contaminants and recycling efficiency aiming at production of sustainable and efficient adsorbents for future society.

2. Materials and methods

2.1. Materials

Carboxymethyl cellulose sodium salt (CMC) (medium viscosity), methacrylic anhydride (94%), sulfuric acid (H_2SO_4; 95–98%), nitric acid (HNO_3; 70%), sodium hydroxide (NaOH), triethylamine (TEA), ethanol (EtOH), *N*,*N*-dimethylformamide (DMF, ≥99.8%), copper sulfate pentahydrate ($CuSO_4 \cdot 5H2O$), poly(ethyleneimine) (PEI) (Mw = 750,000, 50% *w*/*v* in H_2O), and methylene blue ($C_{16}H_{18}ClN_3S$; ≥82%) were purchased from Sigma-Aldrich. Sodium lignosulfonate (SLS) (Mw = 20,300; PDI = 2.34; 5–7% 91 methoxy content, <6% water) was purchased from Tokyo Chemical Industry UK Ltd. The water-soluble photo-initiator, modified bis(mesitoyl) phosphinic acid (BAPO-OH), was synthesized by following the procedure reported in literature [45].

2.2. Carboxymethyl cellulose functionalization

The methacrylation of carboxymethyl cellulose sodium salt (CMC) and full characterization of the methacrylated products were presented earlier [30]. Briefly, 2.00 g of CMC was dissolved in 100 mL of water at 50 °C. After cooling the solution at 0 °C, 4 mL of methacrylic anhydride (MA) was added dropwise to the CMC solution and the reaction was continued for 24 h at 0 °C. The pH was periodically adjusted to 8.0 with 3 N NaOH during the entire duration of the reaction. The resulting mixture was precipitated and washed with ethanol to remove the unreacted methacrylic acid and methacrylic anhydride. After 3 days of dialysis against water, the methacrylated product (M-CMC) was freeze dried for two days. Degree of methacrylation was determined by ^1H NMR, which indicated that more than 25% of the hydroxyl groups present in the CMC were successfully methacrylated [30].

2.3. Preparation of SLS derived nano-graphene oxide (nGO)-type carbon dots

Sodium lignosulfonate was carbonized to carbon flakes (CF) via microwave-assisted hydrothermal carbonization (MAHC) reaction, according to our previously reported procedure [44]. Briefly, 2 g of SLS was mixed with 20 mL of 0.01 g/mL aqueous H_2SO_4 solution in a 100 mL Teflon vessel. The MAHC process was performed in a Milestone FlexiWAVE microwave oven. The temperature of the solution was first increased to 240 °C under a ramp time of 20 min and then kept at 240 °C by input irradiation for 2 h (Max power 1200 W). The resulting CF were filtered from the solution, washed with deionized water, and freeze dried for 2 days. For the preparation of nGO-type carbon dots, the CF were oxidized [13,42]. 20 mL of carbon flakes in 70% HNO_3 aqueous solution (1:100 *w*/w) was added into a 100 mL single-neck round-bottom flask and sonicated for 30 min at room temperature. The oxidation was performed by heating the sonicated solution in an oil bath at 90 °C with constant stirring for 30 min. Then, the solution was poured in 60 mL cold deionized water (15 °C) to stop the reaction. The acidic solvent was removed by rotary evaporation and the resulting brownish solid was dried in vacuum oven for one week.

2.4. Synthesis of methacrylated nGO (M-nGO) carbon dots

The nGO was functionalized by methacrylation [43]. 50 ml of 1 mg/mL DMF/nGO solution was poured into 250 mL single-neck round-bottom flask. The solution was sonicated for 1 h. Next, TEA (10 ml) was added and the solution was stirred for 1 h at room temperature. Subsequently, the temperature was increased to 70 °C and 50 mL of a mixture of MA/DMF 10% (*v*/v) was added dropwise to the nGO containing solution. The final solution was kept at 70 °C for 24 h. At the end of the reaction, the solvent was removed by rotary evaporation and methacrylated nGO (M-nGO) was recovered. M-nGO were further washed with EtOH and centrifugated at 8700 rpm to remove any trace of DMF and non-reacted MA. The purification procedure was repeated twice. M-nGO were freeze-dried for 3 days.

2.5. Preparation of hydrogels

First, nGO or M-nGO were dispersed in 5 mL of water at 1, 3 or 5 wt% (with respect to M-CMC). The solutions were sonicated for 1 h, after which the remaining aggregated nanoparticles were broken down by ultra-turrax homogenizer during 15 min. The temperature of the solution was increased to 50 °C and 100 mg of M-CMC was added. The solution was stirred for 1 h at 50 °C. After cooling down, 2 wt% of photo-initiator BAPO-OH was added to the solution and the mixture was stirred for additional 30 min in the dark. The hydrogel nanocomposites were photo-cured for 5 min by UV-DIMAX lamp with a light intensity of 115 mW/cm^2. The hydrogel nanocomposites were named CMC/nGOX or CMC/M-nGOX, where "X" represents the wt% of nGO or M-nGO, respectively.

2.6. Swelling test

The swelling ability of the photo-cured and freeze-dried CMC hydrogel nanocomposites was evaluated. The dried hydrogel nanocomposites were immersed in deionized water at room temperature for 24 h. The swelling degree (SD) was determined using the following equation:

$$SD\ (\%) = \left(\frac{W_f - W_0}{W_0}\right) * 100$$

where W_f is the final weight and W_0 is the weight of the dry sample. The results of the swelling degree were averaged over measurements carried out on three different samples.

2.7. Adsorption and desorption tests

2.7.1. Methylene blue (MB) adsorption/desorption

MB adsorption experiments were carried out by adding 8 mL of MB solution (65 mg/L) to 3 mg of dry hydrogel in a water bath at room temperature. The pH of the MB solution was adjusted to pH 9 to maximize dye adsorption with drop-wise additions of 0.01 M NaOH. Then, the solution was agitated at 240 rpm by rotary shaker. Dye adsorption was carried out under dark conditions to prevent photocatalytic degradation of methylene blue. In order to monitor dye adsorption, 100 μL of supernatant was continuously taken out from the mixture at specific time intervals (0, 3, 8, 18, 33, 63, 123, 243, 483, 1440 min), respectively. The supernatant was diluted with 1.5 mL water, and the maximum absorbance was measured by UV–vis absorption spectrophotometer ($\lambda = 663$ nm). The amount of adsorbed dye was then calculated. After the adsorption process, the hydrogel nanocomposites were kept in 80 mL HCl for 24 h for desorption of the dye (pH = 2). The solution was agitated at 240 rpm by rotary shaker. Finally, the hydrogel was washed overnight in 50 mL deionized water and freeze-dried for 2 days.

2.7.2. Cu (II) adsorption/desorption

Copper adsorption experiments were carried out by mixing 6 mL Cu (II) solution (300 mg/L, $CuSO_4{\cdot}5H_2O$ 0.0012 M) with 3 mg hydrogel in a water bath at room temperature. The pH values of all solutions were adjusted to pH 5.2 with drop-wise addition of 0.01 M NaOH or HCl. Then, the solution was agitated at 240 rpm by rotary shaker. In order to monitor the concentration of Cu(II) in solution, 100 μL supernatant was continuously taken out from the mixture at specific time intervals (0, 5, 15, 30, 60, 120, 240, 1440 min), respectively. For each time interval, 100 μL of copper solution was extracted from the medium and diluted with 3.8 mL of water. Then, 100 μL of aqueous poly(ethyleneimine) (PEI) solution (90 mg/mL) was added to the mixture to form a cuprammonium complex. This complex allows Cu(II) ions to be detected by UV–vis absorption spectrophotometer ($\lambda = 625$ nm) [13]. After copper adsorption, the hydrogel nanocomposites were regenerated in 30 mL of EDTA solution (0.01 M) for 24 h. Finally, the hydrogels were washed overnight in 50 mL deionized water and freeze-dried for 2 days. The adsorption capacity of the hydrogels at time t (q_m, mg/g) and the equilibrium adsorption capacity (q_e, mg/g) were calculated based on the changes in the MB/Cu(II) concentration before and after adsorption, according to the following equations, respectively:

$$q_m = \frac{(C_0 - C_t) * V}{m}$$

$$q_e = \frac{(C_0 - C_e) * V}{m}$$

where C_0 and C_t (mg/L) are the concentrations of MB/Cu(II) solutions at the initial time and at time t (min), respectively; C_e (mg/L) is the equilibrium concentration of MB/Cu(II) solution; V (L) is the volume of the MB/Cu(II) solution, and m (g) is the weight of the dried hydrogel.

2.8. Recycling test

The Cu(II) and MB adsorption-desorption procedures were repeated three times. In order to evaluate the reusability of the hydrogel nanocomposites, q_e (mg/g) was calculated for each new adsorption cycle. Moreover, the recycling efficiency R (%) of regenerated hydrogel nanocomposites was calculated as follows:

$$R(\%) = \frac{q_n}{q_1} * 100$$

where q_n is the adsorption capacity of the hydrogel in the n^{th} cycle, and q_1 is the adsorption capacity of the hydrogel in the first cycle. Thus, the adsorption capacity of the hydrogels in the first cycle is set as 100%.

2.9. Characterization

Fourier transform infrared spectroscopy (FT-IR) was carried out by PerkinElmer Spectrum 2000 FTIR spectrometer equipped with attenuated total reflectance (ATR) accessory (Graseby Sperac). All spectra were recorded in the wavenumber range of 4000–600 cm^{-1}. Confocal Raman measurements were conducted on a HR800 UV Jobin Yvon Raman spectrometer (Horiba Scientific, Ltd.) with a solid-state laser set at an excitation wavelength of 514 nm. The thermal decomposition profiles of the carbon products were investigated through thermogravimetric analysis (TGA) by Mettler-Toledo TGA/SDTA instrument. High-resolution images were acquired on an ultrahigh resolution field emission scanning electron microscope, FE-SEM Hitachi S-4800. The SEM samples were coated with 2 nm of platinum/palladium (Pt/Pd) film using a Cressington 208HR Sputter Coater (Cressington Scientific Instruments, Ltd.). Elemental analysis was performed via energy-dispersive x-ray spectroscopy (EDX) measurements on Pt/Pd-coated samples using an X-MaxN 80 Silicon Drift Detector (Oxford Instruments) attached to the Hitachi SEM S-4800. The quantitative EDX measurements were performed by point analysis of randomly selected sites on the specimen. The elemental compositions are given as an average of 10 point analysis measurements for each sample.

X-Ray Photoelectron Spectroscopy (XPS) spectra were collected by a Kratos Axis Ultra DLD electron spectrometer using mono-chromated Al Ka source operated at 150 W. Pass energy of 160 eV was applied for the wide spectra analyzer and pass energy of 20 eV for the individual photoelectron lines. The surface potential was stabilized by the spectrometer charge neutralization system. The binding energy (BE) scale was referenced to the C1s line of aliphatic carbon, set at 285.0 eV. Processing of the spectra was accomplished with the Kratos software. Rheological and photo-rheological analyses were performed by rheometer DHR-2 (TA instrument) with disposable smooth aluminum parallel plates (diameter of 20 mm). The frequency sweep technique was utilized to measure the storage and loss modulus of the crosslinked hydrogel nanocomposites. The frequency was varied from 0.01 to 10 Hz at constant applied strain of 1% and at room temperature. Photo-rheological tests were performed by coupling the rheometer with UV light emitting diode (LED) arrays (365 nm, max intensity 150 mW/m^2). The hydrogel nanocomposite formulations were prepared and set down on a quartz plate (20 mm diameter). After setting the gap at 1 mm, the light source was turned on with a delay of 60 s respect to the beginning of the experiment. Variations in storage and loss modulus were recorded as function of time with a constant angular frequency (6.28 rad/s) and constant applied strain (0.1%). UV–vis absorption spectrophotometer (Shimadzu UV-2550) was used to evaluate the concentration of Cu(II) and MB in solution after the adsorption experiments.

3. Results and discussion

"All-lignocellulose" derived photo-curable hydrogel nanocomposites consisting of methacrylated carboxymethyl cellulose (CMC) and carbonized sodium lignosulfonate (SLS)-derived nano-graphene oxide (nGO) carbon dots were designed for adsorption of cationic contaminants (Fig. 1).

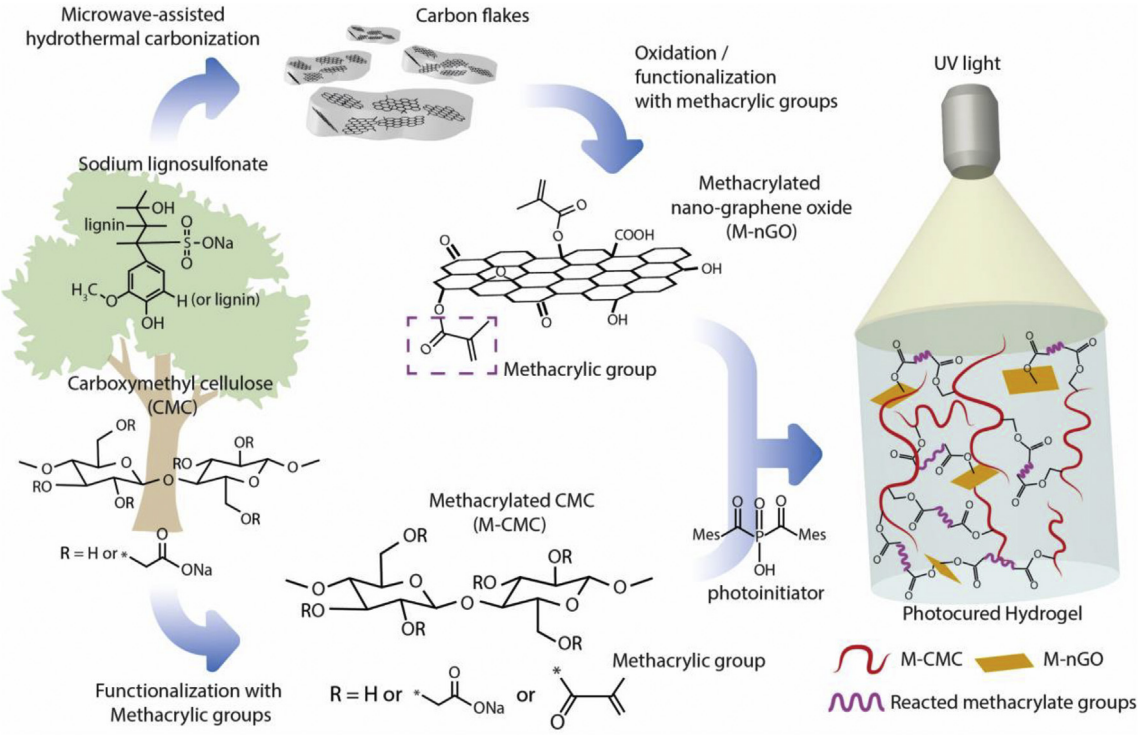

Fig. 1. Schematic illustration showing the preparation steps for the hydrogel nanocomposite M-CMC/M-nGO.

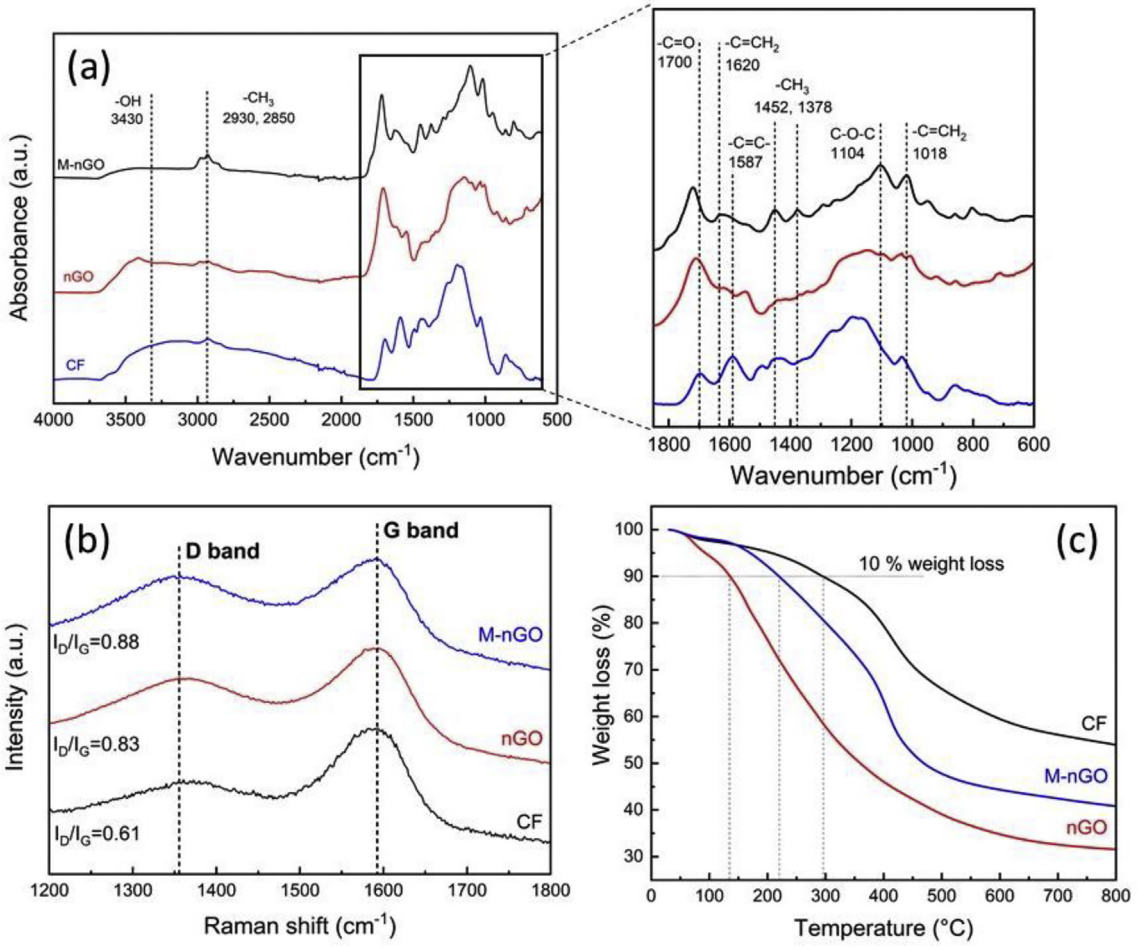

Fig. 2. (a) FTIR spectra of CF, nGO and M-nGO; (b) confocal Raman spectra of CF, nGO, and M-nGO; (c) TGA of CF, nGO, and M-nGO.

3.1. Preparation of nGO and methacrylated M-nGO

Our previous study showed that under relatively mild conditions ($T = 240$ °C) and microwave irradiation, SLS undergoes solid-solid conversion involving partial aromatization and dehydration [44]. The obtained carbon products, denoted as carbon flakes (CF), possessed an elongated shape (100 to 700 nm in length) and thickness around 5 nm. CF consisted of nano-graphitic domains surrounded by various defects including oxygenated groups, sp^3 hybridized carbons, aliphatic side chains, and porosity. Here, two further steps were implemented: i) CF oxidation to produce nGO, and ii) nGO functionalization with methacrylate groups.

As already reported for similar biomass-derived carbon products [42], oxidation can disassemble the carbon sphere or carbon flake structures releasing small highly oxygenated nGO dots. Here, we utilized methacrylic anhydride as methacrylation agent to further functionalize nGO to methacrylate-functionalized M-nGO. The chemical modification that transformed CF to nGO and M-nGO was confirmed by several spectroscopic tools, including Raman spectroscopy, Fourier transform infrared spectroscopy (FTIR), X-ray photoelectron spectroscopy (XPS), confocal Raman, as well as thermogravimetric analysis (TGA).

FTIR spectra of CF, nGO and M-nGO were collected to identify and confirm the chemical functionalities of each product (Fig. 2a). The CF spectrum confirmed the aromatization achieved during the MAHC process. The presence of aromatic rings was signaled by the band at 1587 cm^{-1}, which is associated to the stretching vibration of C═C [44]. C═O stretching vibration in CF was identified at 1700 cm^{-1}. The C═O carbonyl band was shifted towards higher wavenumber for nGO (1711 cm^{-1}) and M-nGO (1720 cm^{-1}), which indicates progressive introduction of carboxylic acid [46] and ester groups, respectively. The presence of methacrylate functionality in M-nGO was confirmed by the bands at 1104 cm^{-1}, vinyl bands (from the methacrylate) at 1620 and 1018 cm^{-1}, and an increased intensity for methyl bands at 1378 and 1452 cm^{-1} (CH_3 bending modes), and 2930 and 2850 cm^{-1} (CH_3 stretching modes). Moreover, the broad peak representing the hydroxyl absorption band around 3430 cm^{-1} was significantly reduced after esterification.

Confocal Raman spectrum of graphitic material is characterized by two characteristic bands named D, and G. The D band is attributed to the scattering from defects, which break the basic symmetry of the sp^2 carbon in graphene sheet. The G-band, instead, arises from planar configuration of the sp^2 bonded carbon in graphene. The Raman spectra in Fig. 2b show a similar pattern for all the three samples. D, and G bands can be easily recognized at 1367, and 1584 cm^{-1}, respectively. The degree of ordering can be estimated by the intensity ratio I_D/I_G. The presence of oxygenated functionalities, sp^3 hybridized carbon, and aliphatic side chains in CF resulted in I_D/I_G ratio around 0.61 [44]. The larger amount of hydroxyl and carboxyl groups in nGO (with respect to CF) contributed to increasing the disorder/defect D band. This consequently increased the intensity ratio to $I_D/I_G = 0.83$. A slight further increase in the I_D/I_G ratio was observed for M-nGO as a result of the esterification reaction.

Thermal degradation of CF, nGO ad M-nGO was investigated by TGA. Fig. 2c illustrates different thermal behaviors for the three carbon materials. Due to the lower density of oxygenated functionalities, CF exhibited higher thermal stability (only 10% weight loss at 294 °C)

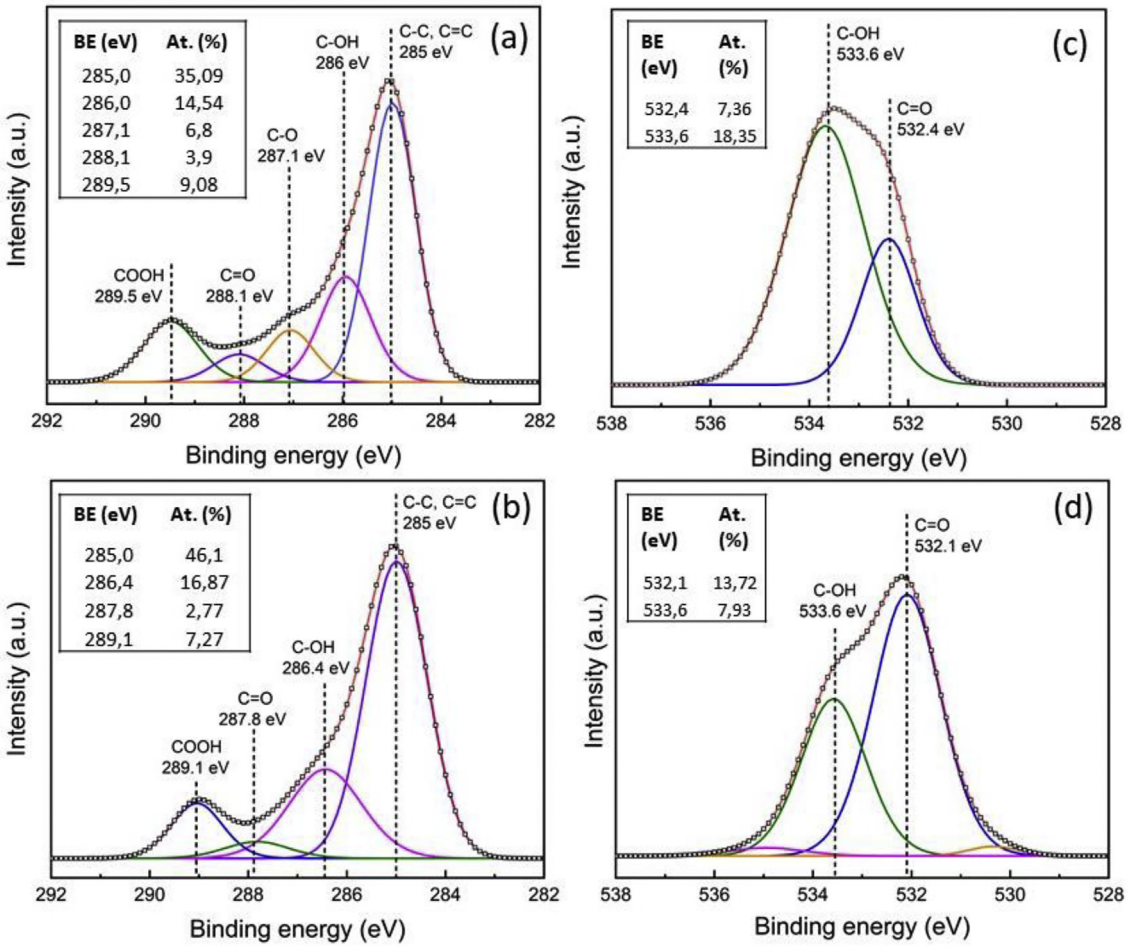

Fig. 3. XPS deconvoluted C 1 s spectra of nGO (a) and M-nGO (b); XPS deconvoluted O 1 s spectra of nGO (c) and M-nGO (d).

with respect to nGO and M-nGO. The maximum weight loss for CF took place approximately between 350 and 500 °C. In this temperature range, the decomposition of unstable oxygenated groups occurred with consequent release of CO and CO_2 [47]. The large remaining residue (54 wt% at 800 °C) is explained by the large amount of stable aromatic structures in CF [13]. All three products, CF, nGO and M-nGO, showed a first decomposition step at relatively low temperature (below 120 °C) due to the adsorbed moisture on their surface. The high amount of oxygenated functionalities (hydroxyl and carboxylic groups) in nGO led to larger initial mass loss. In accordance with previous works [41], the oxygenated functionalities reduced the thermal stability of nGO. This resulted in 10% weight loss at 136 °C and reduced residue content at 800 °C (31 wt%). The methacrylate functionalization of M-nGO contributed to partially recovered thermal stability [48] in comparison with nGO. M-nGO and CF show a similar trend with a maximum weight loss between 350 and 500 °C. In comparison with CF, M-nGO exhibited reduced thermal stability (10% weight loss at 220 °C), which is explained by the remaining carboxylic and hydroxyl groups and by reduced aromatic content in comparison with CF.

The nGO and M-nGO functionalization was further investigated by XPS (Fig. 3). The C 1 s spectra showed the characteristic signals of nGO as identified in previous studies for cellulose and chitosan derived nGO [42,49]. These include aliphatic/aromatic carbon groups C-C/C=C/C-H_x (285 eV), C-OH (286 eV), -C-O (287.1 eV), C=O (288.1 eV), and COOH (289.5 eV) (Fig. 2a). Comparison of the XPS spectrum of nGO and the XPS spectrum of CF reported in our previous paper [44], showed that the oxidation reaction led to an increase in the at.% of hydroxyl and carboxyl groups on the nGO surface. After esterification of nGO, an increase in at.% of aliphatic groups (vinyl and methyl) was reported for the peak at 285 eV (Fig. 3b). Successful methacrylation of nGO was further confirmed by O 1 s (Fig. 3d). The C-OH and C=O groups in nGO correspond to peaks at 533.6 and 532.4 eV, respectively. After the esterification reaction, the at.% of C-OH in M-nGO (533.6 eV) decreased with respect to the same peak in nGO. On the other hand, the at.% of C=O in M-nGO (532.1 eV) increased, which strongly indicates the presence of methacrylate groups on the nGO surface.

3.2. Photo-curable hydrogel nanocomposite

The synthesis and characterization of methacrylated CMC and its fast photo-curing ability was reported in our previous paper [30]. Here, a formulation of M-CMC resin with BAPO-OH initiator was prepared and FT-IR spectra was collected before and after the photo-curing reaction. Upon UV light, BAPO-OH initiator undergoes to Norrish type I cleavage generating two free mesityl radicals [50]. Both radicals efficiently initiate the methacrylate double bonds, thereby promoting the formation of a crosslinked network (Fig. 1). Similar radical crosslinking reactions under UV light have been reported for methacrylated bio-based polymers including gelatin [51], starch [52], and chitosan [43,53]. Successful photo-curing is indicated by the spectra in Fig. 4a, as the double bond related to the -C-H band at 811 cm^{-1} was drastically reduced after 5 min of visible light irradiation. These two spectra were normalized with respect to the C=O vibration band at 1711 cm^{-1}, which is expected to remain unchanged during the photo-curing process. The photo-reactivity of the M-CMC/BAPO-OH resin formulation was further confirmed by photo-rheology. The storage (G') and loss modulus (G") were monitored during the UV-curing process (Fig. 4b). Once the light was turned on at $t = 60$ s, the moduli variations were recorded as a function of time. The maximum conversion of the methacrylate double bonds was attained after 120 s corresponding to the plateau

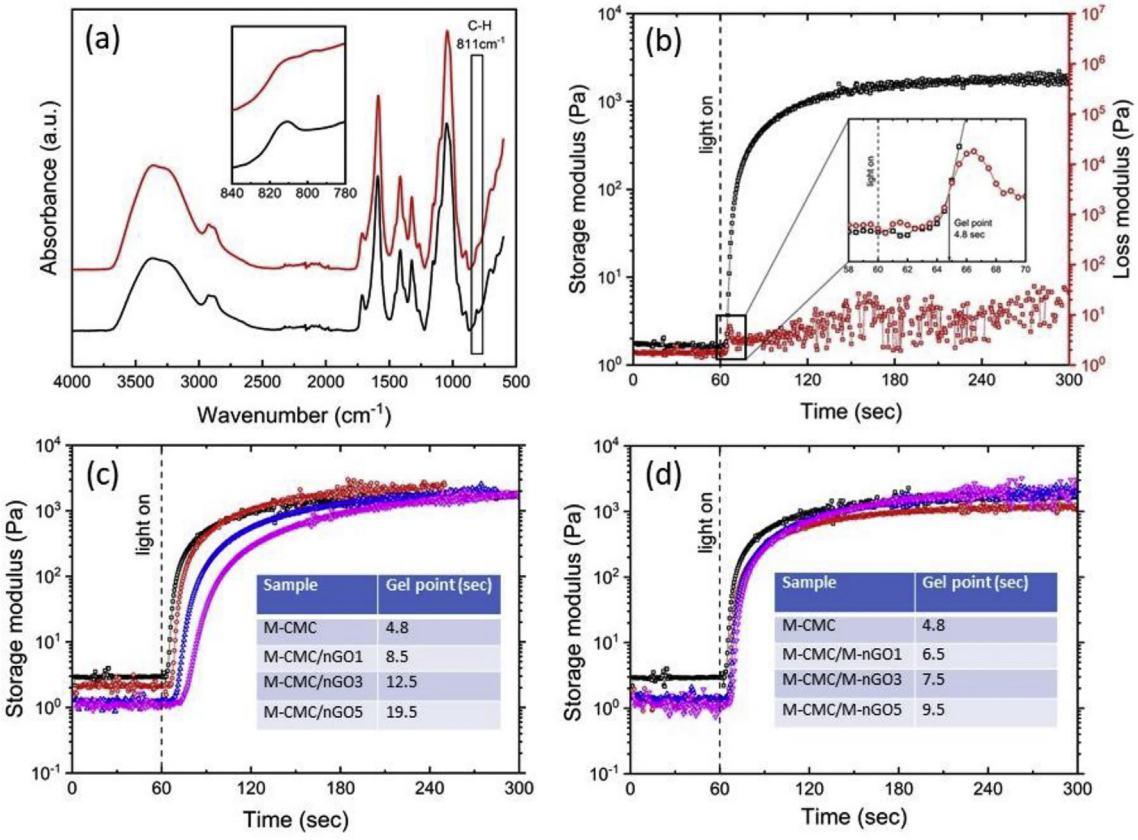

Fig. 4. (a) FT-IR spectra of M-CMC before and after photo-curing and (b) photo-rheology of the M-CMC/BAPO formulation. Photo-rheology of the hydrogel nanocomposites: (c) M-CMC (□), M-CMC/nGO1 (○), M-CMC/nGO3 (△), M-CMC/nGO5 (▽) and (d) M-CMC (□), M-CMC/M-nGO1 (○), M-CMC/M-nGO3 (△), M-CMC/M-nGO5 (▽).

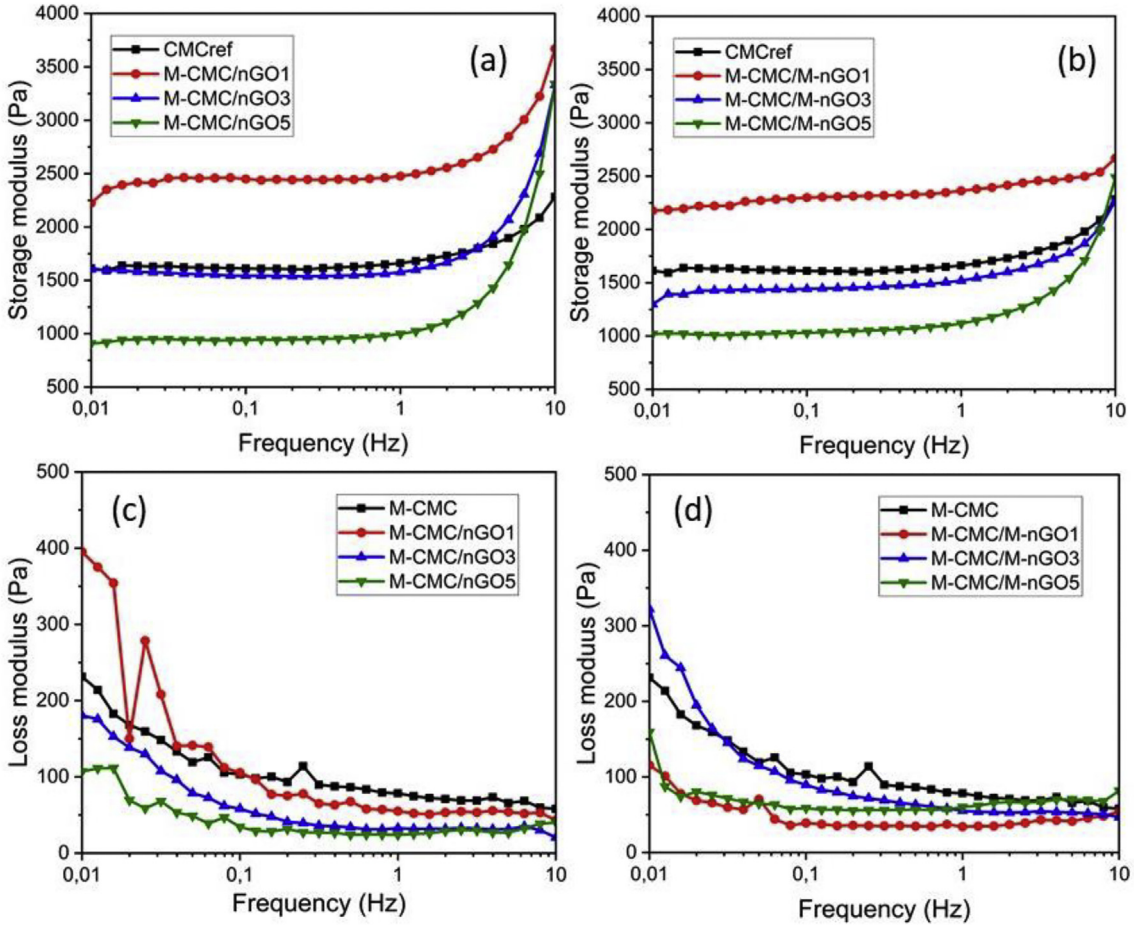

Fig. 5. Storage modulus vs frequency of (a) M-CMC/nGOX and (b) M-CMC/M-nGOX; Loss modulus vs frequency of (c) M-CMC/nGOX and (d) M-CMC/M-nGOX (X = 1,3 and 5 wt% of nGO or M-nGO).

value of the storage modulus G'. The transition from the liquid resin to solid polymer network is defined as the gel point. This time point is given by the intersection between G' and G" during the photo-crosslinking reaction. The inset in Fig. 4b reveals a gel point of 4.8 s, which is in line with the gel point of a similar formulation consisting of M-CMC and lithium phenyl(2,4,6-trimethylbenzoyl) phosphinate (LAP) photo-initiator [30].

The hydrogel nanocomposites were prepared by adding 1, 3 or 5 wt% of nGO or M-nGO into the M-CMC/BAPO-OH reference formulation. The influence of nGO and M-nGO on the photo-curing properties of the hydrogels was investigated by photo-rheology. The storage modulus of the different compositions was recorded as a function of time. All the tested hydrogel nanocomposites were compared with the reference formulation M-CMC. As reported in Fig. 4 c,d the presence of nanoparticles entailed a delay in the photo-curing reaction. This delay was quantified through the gel point measurements. Due to the screening effect, nanoparticles limited the light penetration through the hydrogel resin formulation, which in turn induced a delay in reaching the gel point for all the tested nanocomposite formulations. The gel point values are reported in the insets of Fig. 4c,d. The delay was substantially smaller in the case of the hydrogel nanocomposites containing M-nGO. This is explained by the fact that the M-nGO nanoparticles are directly involved in the photo-curing process of the hydrogel nanocomposites, creating covalent crosslinks with the methacrylated CMC matrix and thereby counteracting the screening effect.

The nanoparticle content affected the final storage modulus of the hydrogel nanocomposites. The frequency sweeps of all M-CMC/nGOX and M-CMC/M-nGOX (X = 1, 3 or 5 wt% nGO or M-nGO) formulations were performed in the linear viscoelastic region. The applied strain was 1%. Regardless of the M-nGO/nGO content, the hydrogel nanocomposites exhibited a larger G' (Fig. 5 a,b) compared with G" (Fig. 5 c,d) by a factor of approximately 30–50. Thus, all the tested hydrogel nanocomposites

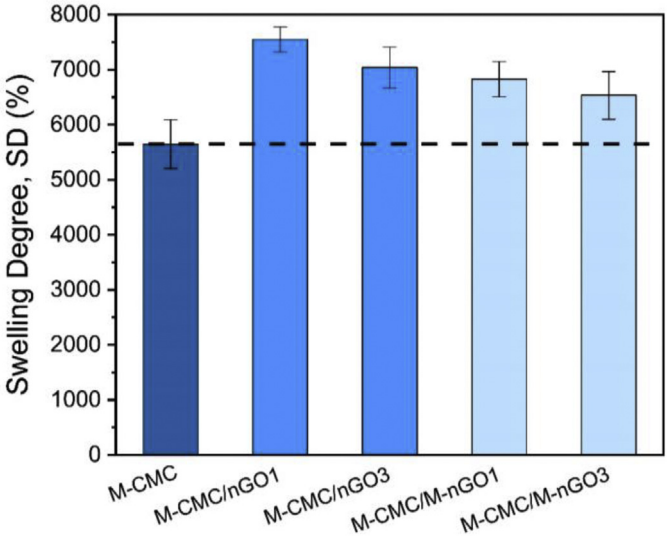

Fig. 6. Swelling degree of M-CMC and the hydrogel nanocomposites M-CMC/nGOX and M-CMC/M-nGOX (X = 1,3 or 5 wt% nGO or M-nGO).

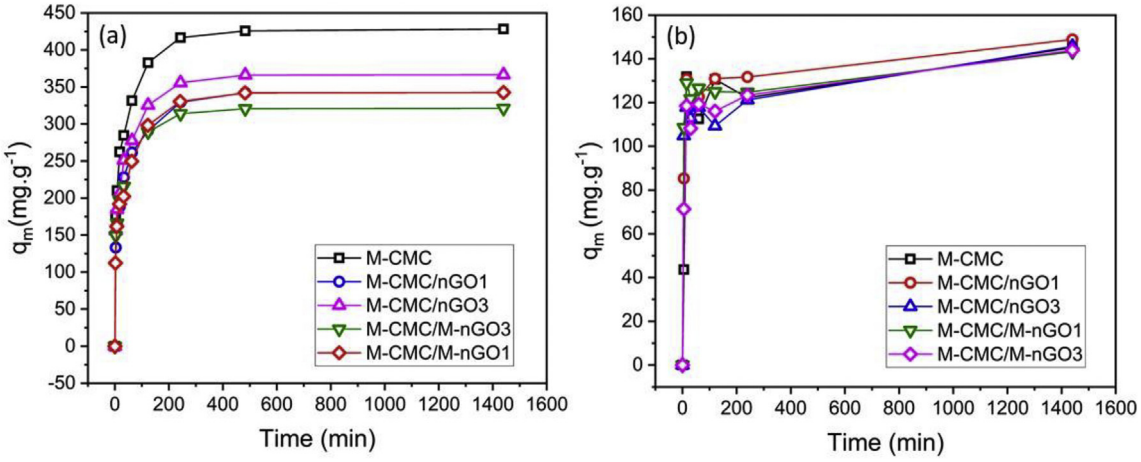

Fig. 7. q_m vs time for (a) MB adsorption (initial concentration 65 mg/L, and (b) Cu(II) adsorption (initial concentration 300 mg/L).

behaved as elastic solids with phase angles (δ) between 0.8 and 3° (Table S1). Low nanoparticle concentration (1 wt% of nGO or M-nGO) entailed an increase of G' in the explored frequency range. The reinforcement effect may be explained by the hydrogen bonding that occurs between the highly oxygenated nanoparticles (nGO/M-nGO) and M-CMC polymer matrix. The methacrylate groups in M-nGO allowed additional covalent linkages with the M-CMC chains. When the amount of nGO and M-nGO increased to 3 and 5 wt%, the probability of nanoparticle aggregation became more likely with a consequently weaker interactions between nGO/M-nGO and M-CMC. This entailed a drop of the G' as shown in Fig. 5 a,b.

The lower mechanical strength and later gel point recorded for M-CMC/M-nGO5 did not allow further testing of the hydrogel nanocomposites with highest content of M-nGO for swelling and heavy metal and dye adsorption. The swelling degrees at equilibrium (SD) of M-CMC and the hydrogel nanocomposites M-CMC/nGOX or M-CMC/M-nGOX (X = 1 or 3 wt% nGO or M-nGO) were measured from the dry state after 24 h at RT in water. As displayed in Fig. 6, the photo-cured M-CMC hydrogel exhibited a SD of 5600%. With respect to the M-CMC hydrogel, the SD of the hydrogel nanocomposites were in the same range. However, the presence of nGO/M-nGO further increased the SD of the hydrogel nanocomposites by 14–26%. At the pH of deionized water, the carboxyl groups in nGO/M-nGO and M-CMC polymer matrix are deprotonated to -COO^-. Under these conditions, the electrostatic repulsion between the CMC and nGO/M-nGO could produce a more expanded network with larger SD [24,54]. Furthermore, the potentially lower degree of crosslinking (due to shielding effect), could also increase the SD. This is supported by the somewhat higher SD values of the nGO composites compared with M-nGO composites. Furthermore, similar effect was also seen previously for methacrylated chitosan modified with nGO, although the swelling degree of chitosan hydrogels was significantly lower [43].

3.3. Methylene blue and copper adsorption

The high amount of oxygenated functional groups such as carboxyl and hydroxyl in the M-CMC network and on the nGO/M-nGO surface made the produced hydrogel nanocomposites good candidates for cationic dye and heavy metal ion adsorption. The hydrogel nanocomposites were, thus, tested as adsorbents for methylene blue (MB) and Cu (II). Fig. 7 a,b display the time dependent adsorption for MB, and Cu (II) on M-CMC/nGOX and M-CMC/M-nGOX (X = 1, 3 wt% of nGO or M-nGO) hydrogel nanocomposites, respectively. As shown in Fig. 7, irrespective of the hydrogel, the amount of adsorbed MB and Cu(II) increased sharply within the first 300 and 120 min, respectively and then gradually started to level off towards the equilibrium value (q_e). The q_e was however affected by the hydrogel composition and the degree of crosslinking [13,14].

The experimental adsorption data were fitted by pseudo-second-order (Fig. S1), demonstrating a high correlation coefficient R^2 (>0.9983) and a calculated adsorption capacity ($q_{e,calc}$) close to the experimental value ($q_{e,\,exp}$) (Table S2,S3). According to this kinetic model, chemisorption is the rate determining step [55]. The pH of the MB and Cu(II) solutions for the adsorption tests were adjusted to 9 and 5.2, respectively. Since the pk_a of carboxyl groups is around 4.6 [54], the use of these pH values provides deprotonated carboxyl groups. The enhanced anionic nature of M-CMC/nGOX/M-nGOX increases the number of the binding sites for the adsorption of cationic MB and Cu(II). Fig. 7a illustrates that the photo-crosslinked M-CMC shows larger MB adsorption capacity, q_m, compared with the hydrogel nanocomposites. This is in contrast with similar work where the use of nGO enhanced the adsorption capacity of the hydrogel by introducing electrostatic and π-π interactions between the nGO surface and the cationic dyes [24,35,56]. One possible explanation might be related to the secondary interaction occuring between the nGO/M-nGO and the polymer matrix. As stated above, low concentration of nanoparticles (1 wt%) improved the storage modulus of the hydrogel nanocomposites. Nevertheless, the same interactions seem to be detrimental for the cationic dye adsorption as the available binding sites might be consumed by formation of secondary interactions between CMC and nGO/M-nGO. This effect was even more evident for the nanocomposites containing 3 wt% of nanoparticles. As shown in Fig. 7b the Cu(II) adsorption was not affected by the

Table 1
maximum adsorption capacity of various adsorbents towards Cu and MB.

Adsorbents	Contaminant	Q_{max} (mg.g^{-1})	Reference
CMC/GO microparticles	MB	59	[24]
	Cu^{2+}	30	
GO/CMC monoliths	Cu^{2+}	70	[56]
Polyvinyl alcohol/Laponite	MB	251	[57]
PVA/CMC/GO/Bentonite	MB	172	[28]
Cellulose/GO fibres	MB	480	[58]
Aminated guar gum/graphene oxide	MB	227	[38]
Soy protein-polyethylenimine	Cu^{2+}	136	[59]
Konjac glucomannan/GO	MB	92.3	[36]
Regenerated cellulose/GO	MB	68	[60]
GO/chitosan	MB	300	[35]
	Cu^{2+}	70	
M-CMC/nGO/M-nGO	MB	350	Present work
	Cu^{2+}	145	

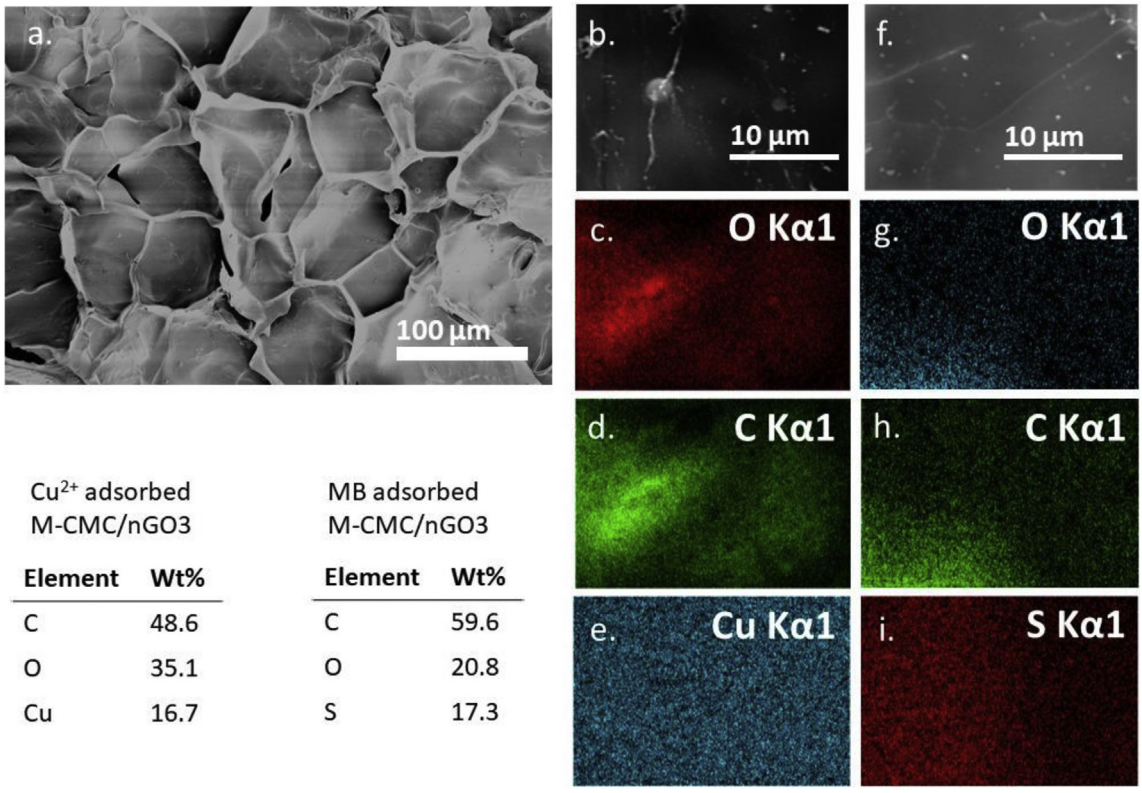

Cu^{2+} adsorbed M-CMC/nGO3

Element	Wt%
C	48.6
O	35.1
Cu	16.7

MB adsorbed M-CMC/nGO3

Element	Wt%
C	59.6
O	20.8
S	17.3

Fig. 8. (a) SEM image of the surface of M-CMC/nGO3; EDX spetra of M-CMC/nGO3 after (b-e) MB, and (f-i) Cu(II) adsoprtion. The inset table shows the EDX quantitative evaluation of C, O, Cu and S for M-CMC/nGO3.

addition of nGO/M-nGO. This might be due to the higher diffusivity and mobility of the Cu(II) with respect to the MB. Even so, the maximum adsorption capacity of the hydrogel nanocomposites M-CMC/nGOX and M-CMC/M-nGOX (X = 1, 3 wt% nGO or M-nGO) under our experimental condition reached high values between 300 and 350 mg/g.

It is interesting to point out that the obtained q_e values (around 430 mg/g for MB, and 145 mg/g for Cu(II)) are larger than the values reported for cellulose-based composite adsorbents in the literature. A selection of comparative adsorption capacities for MB and Cu(II) are summarized in Table 1.

The adsorption of MB and Cu(II) was also confirmed by EDX. After adsorption, the samples were directly dried for two days by freeze-drying. The dried nanocomposites were coated with a thin layer of Pt/Pd prior to EDX analysis. The SEM image of the M-CMC hydrogel is shown in Fig. 8a. The hydrogel surface displays a high degree of porosity with pore sizes between 10 and 50 µm. The presence of nGO and M-nGO in the hydrogels did not seem to affect the pore size of the nanocomposite (Fig. S2). Fig. 8 shows as an example the MB and Cu(II) adsorption on M-CMC/nGO3 nanocomposite. No evident adsorption inhomogeneity was observed among the different hydrogel nanocomposites and the M-CMC hydrogel. The adsorption of MB and Cu(II) on the nanocomposite surfaces were identified through the presence of sulphur and copper elements. Sulphur was chosen as a marker because it is present in MB. Preliminary EDX investigations were conducted on neat M-CMC

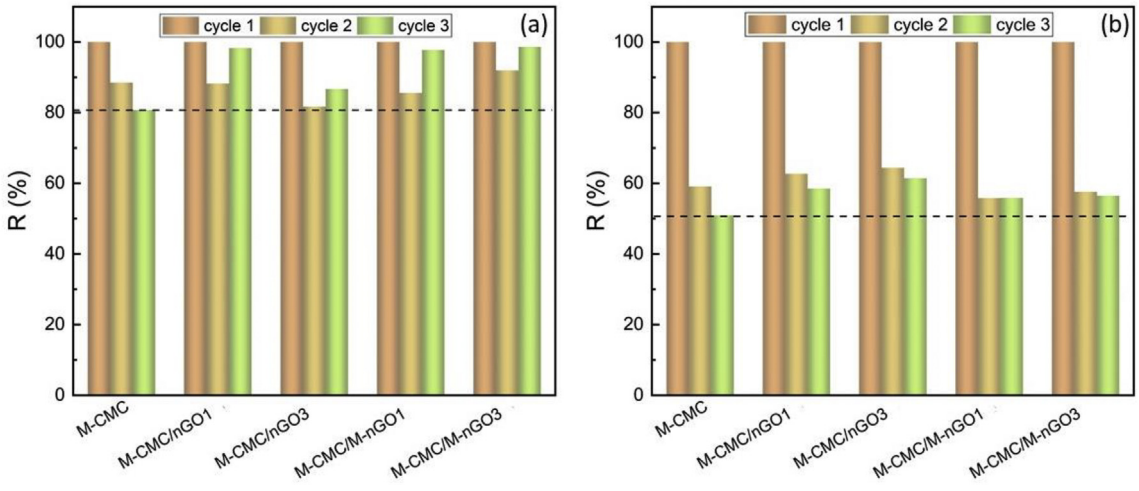

Fig. 9. recycling efficiency (R%) of the hydrogels for (a) MB, and (b) Cu(II) adsorption.

and nGO/M-nGO to prove the absence of sulphur and copper. Two EDX spots were reported after adsorption of Cu (Fig. 8b-e) and MB (Fig. 8f-i) in M-CMC/nGO3 nanocomposites. The images illustrate homogeneous distribution of adsorbed Cu (Fig. 8e), and MB (Fig. 8i) on the surface of the hydrogel nanocomposite. The percentage of Cu and S on the surface of the hydrogels was measured to be around 16.7 and 17.3%, respectively.

3.4. Hydrogel regeneration

For efficient water treatment, the regeneration and reuse of adsorbents is a key element. To evaluate the economic feasibility and reusability of the developed hydrogel nanocomposite adsorbents for practical applications, the possibility to desorb MB and Cu from the hydrogel nanocomposites and reuse the hydrogels was evaluated. Three adsorption and desorption cycles were performed on the M-CMC/M-nGOX (X = 1, 3 wt% nGO or M-nGO) hydrogel nanocomposites. Each cycle of adsorption was followed by a desorption step. Two different strategies were used to regenerate the hydrogel nanocomposites depending on the adsorbed contaminant. The regeneration of the hydrogel nanocomposites after copper adsorption was performed in EDTA solution (0.01 M). The chelating agent effectively removed copper from the hydrogels. Aqueous HCl solution (pH = 2) was used to regenerate the hydrogel nanocomposite after the MB adsorption.

As shown in Fig. 9, the recycling efficiency R (%) of the M-CMC hydrogel decreased after three cycles from the initial value of 100% to 80% for MB and to 50% for Cu(II), indicating adequate reusability for MB and Cu(II) removal. With respect to M-CMC, the hydrogel nanocomposites exhibited enhanced R(%) after 3 cycles. This was observed both during MB (Fig. 9a) and Cu(II) (Fig. 9b) adsorption. Unlike the first cycle, where the q_m of the nanocomposites were slightly lower (Fig. 7a) or comparable (Fig. 7b) with the M-CMC hydrogel, the presence of the nanoparticles had a beneficial effect on the regeneration.

4. Conclusions

"All-lignocellulose" derived photo-curable hydrogel nanocomposites consisting of methacrylated-CMC/lignin-derived nGO, were successfully designed and tested for adsorption of cationic contaminants. The fabricated hydrogel nanocomposites demonstrated outstanding adsorption capacity and good recycling efficiency. Lignosulfonate-derived nano-graphene oxide was successfully produced through microwave-assisted hydrothermal carbonization of lignosulfonate to carbon flakes followed by oxidation step. The high amount of oxygen functionalities in nGO allowed further functionalization by introduction of photo-reactive methacrylate groups. The successful methacrylation of nGO was proven by several spectroscopic techniques including XPS, and FTIR. All formulations showed good photo-curing properties, however, the addition of nGO increased the time required for reaching the gel point. This effect increased as a function of increasing nGO content due to the shielding effect generally observed for aromatic compounds. Unlike nGO, M-nGO participated in the photo-curing process creating chemical crosslinks with the M-CMC polymer matrix under UV light. This reduced the shielding effect and shortened the time required for reaching the gel point. A low content (< 3 wt%) of nGO, and M-nGO in the M-CMC nanocomposites provided a substantial increase of the storage modulus and swelling degree with respect to the neat M-CMC hydrogel. The photo-cured M-CMC hydrogel, M-CMC/nGO and M-CMC/M-nGO hydrogel nanocomposites demonstrated excellent adsorption capacities (up to 350 mg/g and 145 mg/g for MB and Cu(II) adsorption, respectively). The presence of nGO/M-nGO in the nanocomposites was beneficial for the regeneration of the hydrogels leading to improved recycling efficiency (R%) after 3 cycles of MB and Cu(II) adsorption.

Declaration of Competing Interest

The authors declare that they have no known competing financial interests or personal relationships that could have appeared to influence the work reported in this paper.

Acknowledgments

Giuseppe Melilli gratefully acknowledges the financial support from The Foundation BLANCEFLOR Boncompagni-Ludovisi, née Bildt.

Appendix A. Supplementary data

Supplementary data to this article can be found online at https://doi.org/10.1016/j.susmat.2020.e00243.

References

[1] A. Boretti, L. Rosa, Reassessing the projections of the world water development report, NPJ Clean Water 2 (2019) 1–6, https://doi.org/10.1038/s41545-019-0039-9.
[2] M.A. Shannon, P.W. Bohn, M. Elimelech, J.G. Georgiadis, B.J. Mariñas, A.M. Mayes, Science and technology for water purification in the coming decades, Nature. 452 (2008) 301–310, https://doi.org/10.1038/nature06599.
[3] M. Liu, Q. Chen, K. Lu, W. Huang, Z. Lü, C. Zhou, S. Yu, C. Gao, High efficient removal of dyes from aqueous solution through nanofiltration using diethanolamine-modified polyamide thin-film composite membrane, Sep. Purif. Technol. 173 (2017) 135–143, https://doi.org/10.1016/j.seppur.2016.09.023.
[4] F. Fu, Q. Wang, Removal of heavy metal ions from wastewaters: a review, J. Environ. Manag. 92 (2010) 407–418, https://doi.org/10.1016/j.jenvman.2010.11.011.
[5] J. Joseph, R.C. Radhakrishnan, J.K. Johnson, S.P. Joy, J. Thomas, Ion-exchange mediated removal of cationic dye-stuffs from water using ammonium phosphomolybdate, Mater. Chem. Phys. 242 (2020) 122488, https://doi.org/10.1016/j.matchemphys.2019.122488.
[6] A. Yaqub, H. Ajab, S. Khan, S. Khan, R. Farooq, Electrochemical removal of copper and lead from industrial wastewater: mass transport enhancement, Water Qual. Res. J. Can. 44 (2009) 183–188, https://doi.org/10.2166/wqrj.2009.020.
[7] G.Y. Zhao, L.J. Liu, J.R. Li, Q. Liu, Efficient removal of dye MB: through the combined action of adsorption and photodegradation from NiFe2O4/Ag3PO4, J. Alloys Compd. 664 (2016) 169–174, https://doi.org/10.1016/j.jallcom.2016.01.004.
[8] N. de C.L. Beluci, G.A.P. Mateus, C.S. Miyashiro, N.C. Homem, R.G. Gomes, M.R. Fagundes-Klen, R. Bergamasco, A.M.S. Vieira, Hybrid treatment of coagulation/flocculation process followed by ultrafiltration in TIO 2 -modified membranes to improve the removal of reactive black 5 dye, Sci. Total Environ. 664 (2019) 222–229, https://doi.org/10.1016/j.scitotenv.2019.01.199.
[9] J. Abdi, M. Vossoughi, N.M. Mahmoodi, I. Alemzadeh, Synthesis of metal-organic framework hybrid nanocomposites based on GO and CNT with high adsorption capacity for dye removal, Chem. Eng. J. 326 (2017) 1145–1158, https://doi.org/10.1016/j.cej.2017.06.054.
[10] M. Kaykhaii, M. Sasani, S. Marghzari, Removal of dyes from the environment by adsorption process, Chem. Mater. Eng. 6 (2018) 31–35, https://doi.org/10.13189/cme.2018.060201.
[11] Z. Zhao, L. Li, G.S. Geleta, L. Ma, Z. Wang, Polyacrylamide-Phytic acid-Polydopamine conducting porous hydrogel for efficient removal of water-soluble dyes, Sci. Rep. 7 (2017) 1–10, https://doi.org/10.1038/s41598-017-08220-6.
[12] F. Liu, S. Chung, G. Oh, T.S. Seo, Three-dimensional graphene oxide nanostructure for fast and efficient water-soluble dye removal, ACS Appl. Mater. Interfaces 4 (2012) 922–927, https://doi.org/10.1021/am201590z.
[13] J. Yao, K. Odelius, M. Hakkarainen, Carbonized lignosulfonate-based porous nanocomposites for adsorption of environmental contaminants, Funct. Compos. Mater. 1 (2020) 5, https://doi.org/10.1186/s42252-020-00008-8.
[14] Z. Feng, T. Danjo, K. Odelius, M. Hakkarainen, T. Iwata, A.C. Albertsson, Recyclable fully biobased chitosan adsorbents spray-dried in one pot to microscopic size and enhanced adsorption capacity, Biomacromolecules. 20 (2019) 1956–1964, https://doi.org/10.1021/acs.biomac.9b00186.
[15] Y. Zhou, J. Lu, Y. Zhou, Y. Liu, Recent advances for dyes removal using novel adsorbents: a review, Environ. Pollut. 252 (2019) 352–365, https://doi.org/10.1016/j.envpol.2019.05.072.
[16] V.K. Gupta Suhas, Application of low-cost adsorbents for dye removal - a review, J. Environ. Manag. 90 (2009) 2313–2342, https://doi.org/10.1016/j.jenvman.2008.11.017.
[17] Z. Shamsollahi, A. Partovinia, Recent advances on pollutants removal by rice husk as a bio-based adsorbent: a critical review, J. Environ. Manag. 246 (2019) 314–323, https://doi.org/10.1016/j.jenvman.2019.05.145.
[18] A. Ayoub, R.A. Venditti, J.J. Pawlak, A. Salam, M.A. Hubbe, Novel hemicellulose-chitosan biosorbent for water desalination and heavy metal removal, ACS Sustain. Chem. Eng. 1 (2013) 1102–1109, https://doi.org/10.1021/sc300166m.
[19] M.H. Sorour, H.A. Hani, H.F. Shaalan, M.M. el Sayed, M.M.H. El-Sayed, Softening of seawater and desalination brines using grafted polysaccharide hydrogels, Desalin. Water Treat. 55 (2015) 2389–2397, https://doi.org/10.1080/19443994.2014.947783.

[20] J. Wang, M. Liu, C. Duan, J. Sun, Y. Xu, Preparation and characterization of cellulose-based adsorbent and its application in heavy metal ions removal, Carbohydr. Polym. 206 (2019) 837–843, https://doi.org/10.1016/j.carbpol.2018.11.059.
[21] Z. Liu, H. Wang, C. Liu, Y. Jiang, G. Yu, X. Mu, X. Wang, Magnetic cellulose-chitosan hydrogels prepared from ionic liquids as reusable adsorbent for removal of heavy metal ions, Chem. Commun. 48 (2012) 7350–7352, https://doi.org/10.1039/c2cc17795a.
[22] S. Thakur, B. Sharma, A. Verma, J. Chaudhary, S. Tamulevicius, V.K. Thakur, Recent progress in sodium alginate based sustainable hydrogels for environmental applications, J. Clean. Prod. 198 (2018) 143–159, https://doi.org/10.1016/j.jclepro.2018.06.259.
[23] A.M. Farag, H.H. Sokker, E.M. Zayed, F.A. Nour Eldien, N.M. Abd Alrahman, Removal of hazardous pollutants using bifunctional hydrogel obtained from modified starch by grafting copolymerization, Int. J. Biol. Macromol. 120 (2018) 2188–2199, https://doi.org/10.1016/j.ijbiomac.2018.06.171.
[24] J. Liu, H. Chu, H. Wei, H. Zhu, G. Wang, J. Zhu, Facile fabrication of carboxymethyl cellulose sodium/graphene oxide hydrogel microparticles for water purification, RSC Adv. 6 (2016) 50061–50069, https://doi.org/10.1039/c6ra06438h.
[25] N. Peng, D. Hu, J. Zeng, Y. Li, L. Liang, C. Chang, Superabsorbent cellulose-clay nanocomposite hydrogels for highly efficient removal of dye in water, ACS Sustain. Chem. Eng. 4 (2016) 7217–7224, https://doi.org/10.1021/acssuschemeng.6b02178.
[26] C.B. Godiya, X. Cheng, D. Li, Z. Chen, X. Lu, Carboxymethyl cellulose/polyacrylamide composite hydrogel for cascaded treatment/reuse of heavy metal ions in wastewater, J. Hazard. Mater. 364 (2019) 28–38, https://doi.org/10.1016/j.jhazmat.2018.09.076.
[27] S. Yang, S. Fu, H. Liu, Y. Zhou, X. Li, Hydrogel beads based on carboxymethyl cellulose for removal heavy metal ions, J. Appl. Polym. Sci. 119 (2011) 1204–1210, https://doi.org/10.1002/app.32822.
[28] H. Dai, Y. Huang, H. Huang, Eco-friendly polyvinyl alcohol/carboxymethyl cellulose hydrogels reinforced with graphene oxide and bentonite for enhanced adsorption of methylene blue, Carbohydr. Polym. 185 (2018) 1–11, https://doi.org/10.1016/j.carbpol.2017.12.073.
[29] H. Yan, W. Zhang, X. Kan, L. Dong, Z. Jiang, H. Li, H. Yang, R. Cheng, Sorption of methylene blue by carboxymethyl cellulose and reuse process in a secondary sorption, Colloids Surf, A Physicochem. Eng. Asp. 380 (2011) 143–151, https://doi.org/10.1016/j.colsurfa.2011.02.045.
[30] G. Melilli, I. Carmagnola, C. Tonda-Turo, F. Pirri, G. Ciardelli, M. Sangermano, M. Hakkarainen, A. Chiappone, DLP 3D printing meets lignocellulosic biopolymers: carboxymethyl cellulose inks for 3D biocompatible hydrogels, Polymers. 12 (2020) 1655, https://doi.org/10.3390/polym12081655.
[31] G. Zhao, J. Li, X. Ren, C. Chen, X. Wang, Few-layered graphene oxide nanosheets as superior sorbents for heavy metal ion pollution management, Environ. Sci. Technol. 45 (2011) 10454–10462, https://doi.org/10.1021/es203439v.
[32] X. Liu, R. Ma, X. Wang, Y. Ma, Y. Yang, L. Zhuang, S. Zhang, R. Jehan, J. Chen, X. Wang, Graphene oxide-based materials for efficient removal of heavy metal ions from aqueous solution: a review, Environ. Pollut. 252 (2019) 62–73, https://doi.org/10.1016/j.envpol.2019.05.050.
[33] T.H. Tu, P.T.N. Cam, L.V.T. Huy, M.T. Phong, H.M. Nam, N.H. Hieu, Synthesis and application of graphene oxide aerogel as an adsorbent for removal of dyes from water, Mater. Lett. 238 (2019) 134–137, https://doi.org/10.1016/j.matlet.2018.11.164.
[34] T.A. Tabish, F.A. Memon, D.E. Gomez, D.W. Horsell, S. Zhang, A facile synthesis of porous graphene for efficient water and wastewater treatment, Sci. Rep. 8 (2018) 1–14, https://doi.org/10.1038/s41598-018-19978-8.
[35] Y. Chen, L. Chen, H. Bai, L. Li, Graphene oxide-chitosan composite hydrogels as broad-spectrum adsorbents for water purification, J. Mater. Chem. A 1 (2013) 1992–2001, https://doi.org/10.1039/c2ta00406b.
[36] L. Gan, S. Shang, E. Hu, C.W.M. Yuen, S.X. Jiang, Konjac glucomannan/graphene oxide hydrogel with enhanced dyes adsorption capability for methyl blue and methyl orange, Appl. Surf. Sci. 357 (2015) 866–872, https://doi.org/10.1016/j.apsusc.2015.09.106.
[37] C. Li, M. She, X. She, J. Dai, L. Kong, Functionalization of polyvinyl alcohol hydrogels with graphene oxide for potential dye removal, J. Appl. Polym. Sci. 131 (2014) https://doi.org/10.1002/app.39872.
[38] E. Jackcina Stobel Christy, S. Gopi, A. Rajeswari, G. Sudharsan, A. Pius, Highly crosslinked 3-D hydrogels based on graphene oxide for enhanced remediation of multi contaminant wastewater, J. Water Process Eng. 31 (2019), 100850. https://doi.org/10.1016/j.jwpe.2019.100850.
[39] U. Sierra, P. Álvarez, C. Blanco, M. Granda, R. Santamaría, R. Menéndez, New alternatives to graphite for producing graphene materials, Carbon. 93 (2015) 812–818, https://doi.org/10.1016/j.carbon.2015.05.105.
[40] B. Hu, Y. Ai, J. Jin, T. Hayat, A. Alsaedi, L. Zhuang, X. Wang, Efficient elimination of organic and inorganic pollutants by biochar and biochar-based materials, Biochar. 2 (2020) 47–64, https://doi.org/10.1007/s42773-020-00044-4.
[41] N.B. Erdal, K.H. Adolfsson, T. Pettersson, M. Hakkarainen, Green strategy to reduced Nanographene oxide through microwave assisted transformation of cellulose, ACS Sustain. Chem. Eng. 6 (2018) 1245–1255, https://doi.org/10.1021/acssuschemeng.7b03566.
[42] K.H. Adolfsson, S. Hassanzadeh, M. Hakkarainen, Valorization of cellulose and waste paper to graphene oxide quantum dots, RSC Adv. 5 (2015) 26550–26558, https://doi.org/10.1039/c5ra01805f.
[43] Z. Feng, M. Hakkarainen, H. Grützmacher, A. Chiappone, M. Sangermano, Photocrosslinked chitosan hydrogels reinforced with chitosan-derived Nanographene oxide, Macromol. Chem. Phys. 220 (2019) 1900174, https://doi.org/10.1002/macp.201900174.
[44] G. Melilli, K.H. Adolfsson, A. Impagnatiello, G. Rizza, M. Hakkarainen, Intriguing carbon flake formation during microwave-assisted hydrothermal carbonization of sodium lignosulfonate, Glob. Challenges. 4 (2020) 1900111, https://doi.org/10.1002/gch2.201900111.
[45] G. Müller, M. Zalibera, G. Gescheidt, A. Rosenthal, G. Santiso-Quinones, K. Dietliker, H. Grützmacher, Simple one-pot syntheses of water-soluble Bis(acyl)phosphane oxide photoinitiators and their application in surfactant-free emulsion polymerization, Macromol. Rapid Commun. 36 (2015) 553–557, https://doi.org/10.1002/marc.201400743.
[46] K.H. Adolfsson, M. Golda-Cepa, N.B. Erdal, J. Duch, A. Kotarba, M. Hakkarainen, Importance of surface functionalities for antibacterial properties of carbon spheres, Adv. Sustain. Syst. 3 (2019) 1800148, https://doi.org/10.1002/adsu.201800148.
[47] V. Loryuenyong, K. Totepvimarn, P. Eimburanapravat, W. Boonchompoo, A. Buasri, Preparation and characterization of reduced graphene oxide sheets via water-based exfoliation and reduction methods, Adv. Mater. Sci. Eng. 2013 (2013) https://doi.org/10.1155/2013/923403.
[48] K.P. Pramoda, H. Hussain, H.M. Koh, H.R. Tan, C.B. He, Covalent bonded polymer-graphene nanocomposites, J. Polym. Sci. Part A Polym. Chem. 48 (2010) 4262–4267, https://doi.org/10.1002/pola.24212.
[49] Z. Feng, A. Simeone, K. Odelius, M. Hakkarainen, Biobased nanographene oxide creates stronger chitosan hydrogels with improved adsorption capacity for trace pharmaceuticals, ACS Sustain. Chem. Eng. 5 (2017) 11525–11535, https://doi.org/10.1021/acssuschemeng.7b02809.
[50] J. Wang, A. Chiappone, I. Roppolo, F. Shao, E. Fantino, M. Lorusso, D. Rentsch, K. Dietliker, C.F. Pirri, H. Grützmacher, All-in-one cellulose nanocrystals for 3D printing of nanocomposite hydrogels, Angew. Chem. Int. Ed. 57 (2018) 2353–2356, https://doi.org/10.1002/anie.201710951.
[51] M.Y. Shie, J.J. Lee, C.C. Ho, S.Y. Yen, H.Y. Ng, Y.W. Chen, Effects of gelatin methacrylate bio-ink concentration on mechano-physical properties and human dermal fibroblast behavior, Polymers. 12 (2020) 1930, https://doi.org/10.3390/POLYM12091930.
[52] C. Noè, C. Tonda-Turo, A. Chiappone, M. Sangermano, M. Hakkarainen, Light processable starch hydrogels, Polymers. 12 (2020) 1359, https://doi.org/10.3390/POLYM12061359.
[53] C. Tonda-Turo, I. Carmagnola, A. Chiappone, Z. Feng, G. Ciardelli, M. Hakkarainen, M. Sangermano, Photocurable chitosan as bioink for cellularized therapies towards personalized scaffold architecture, Bioprinting. 18 (2020), e00082. https://doi.org/10.1016/j.bprint.2020.e00082.
[54] M.F.A. Taleb, H.L. Abd El-Mohdy, H.A. Abd El-Rehim, Radiation preparation of PVA/CMC copolymers and their application in removal of dyes, J. Hazard. Mater. 168 (2009) 68–75, https://doi.org/10.1016/j.jhazmat.2009.02.001.
[55] D. Robati, Pseudo-second-order kinetic equations for modeling adsorption systems for removal of lead ions using multi-walled carbon nanotube, J. Nanostructure Chem. 3 (2013) 1–6, https://doi.org/10.1186/2193-8865-3-55.
[56] Y. Zhang, Y. Liu, X. Wang, Z. Sun, J. Ma, T. Wu, F. Xing, J. Gao, Porous graphene oxide/carboxymethyl cellulose monoliths, with high metal ion adsorption, Carbohydr. Polym. 101 (2014) 392–400, https://doi.org/10.1016/j.carbpol.2013.09.066.
[57] G.R. Mahdavinia, M. Soleymani, M. Sabzi, H. Azimi, Z. Atlasi, Novel magnetic polyvinyl alcohol/laponite RD nanocomposite hydrogels for efficient removal of methylene blue, J. Environ. Chem. Eng. 5 (2017) 2617–2630, https://doi.org/10.1016/j.jece.2017.05.017.
[58] L. Chen, Y. Li, S. Hu, J. Sun, Q. Du, X. Yang, Q. Ji, Z. Wang, D. Wang, Y. Xia, Removal of methylene blue from water by cellulose/graphene oxide fibres, J. Exp. Nanosci. 11 (2016) 1156–1170, https://doi.org/10.1080/17458080.2016.1198499.
[59] J. Liu, D. Su, J. Yao, Y. Huang, Z. Shao, X. Chen, Soy protein-based polyethylenimine hydrogel and its high selectivity for copper ion removal in wastewater treatment, J. Mater. Chem. A 5 (2017) 4163–4171, https://doi.org/10.1039/c6ta10814h.
[60] F. Ren, Z. Li, W.Z. Tan, X.H. Liu, Z.F. Sun, P.G. Ren, D.X. Yan, Facile preparation of 3D regenerated cellulose/graphene oxide composite aerogel with high-efficiency adsorption towards methylene blue, J. Colloid Interface Sci. 532 (2018) 58–67, https://doi.org/10.1016/j.jcis.2018.07.101.